ACS APPLIED ELECTRONIC MATERIALS

Article

Controlled Construction of Atomic Point Contact with 16 Quantized Conductance States in Oxide Resistive Switching Memory

Qilai Chen, Gang Liu, Wuhong Xue, Jie Shang, Shuang Gao, Xiaohui Yi, Ying Lu, Xinhui Chen, Minghua Tang, Xuejun Zheng, and Run-Wei Li

ACS Appl. Electron. Mater., **Just Accepted Manuscript** • DOI: 10.1021/acsaelm.9b00191 • Publication Date (Web): 24 Apr 2019

Just Accepted

ACS Publications

is published by the American Chemical Society. 1155 Sixteenth Street N.W., Washington, DC 20036

Controlled Construction of Atomic Point Contact with 16 Quantized Conductance States in Oxide Resistive Switching Memory

Qilai Chen,[†,‡,§,∥] *Gang Liu,**[,‡,§] *Wuhong Xue,*[‡] *Jie Shang,*[‡] *Shuang Gao,*[‡] *Xiaohui Yi,*[‡] *Ying Lu,*[‡] *Xinhui Chen,*[‡] *Minghua Tang,*[∥] *Xuejun Zheng,**[,†] *and Run-Wei Li**[,‡]

[†]School of Mechanical Engineering, Xiangtan University, Xiangtan, Hunan 411105, China

[‡]CAS Key Laboratory of Magnetic Materials and Devices, Ningbo Institute of Materials Technology and Engineering, Chinese Academy of Sciences, Ningbo, Zhejiang 315201, China

[§]School of Chemistry and Chemical Engineering, Shanghai Jiao Tong University, Shanghai, 200240, China

[∥]School of Materials Science and Engineering, Xiangtan University, Xiangtan, Hunan, 411105, China

KEYWORDS: resistive switching, SPM, atomic point contact, quantum conductance, hafnium oxide

ABSTRACT: Resistive switching device with controlled formation and evolution of conductive filament possesses great capability of being miniaturized to atomic scale for the construction of high-density memory arrays and even in-memory computing architectures. Although the switching mechanism based on ion migration and electrochemistry has been clarified, precise control of their evolution dynamics is still a challenge that hinders the direct application of the memory devices. In this contribution, we propose an effective scanning probe microscope tip-assisted approach for the performance modulation of oxide based resistive switching devices. The directional migration of oxygen anions inside the hafnium oxide nanofilm is regulated by using the voltage-biased scanning probe microscope (SPM) tip as a microelectrode, so that single filament would be formed deliberately inside the switching matrix to improve the stability and reliability of the memory device greatly. The variations of the switching parameters, e.g. programming voltages and ON/OFF resistances, have been reduced by at least 33%. More importantly, the elaborate tuning of the filament dimension also gives rise to single atomic point contact in the resistive switching device, producing at least 16 half-integer multiples of quantized conductance states that can be used for multilevel data storage and high order neuromorphic computing paradigm.

INTRODUCTION

The approaching end of Moore's Law in the foreseeable future greatly inspires the exploration of novel information storage technique that can go beyond the 10 nanometer node.[1,2] One important attempt is the recently widely studied resistive switching memory, in which the nanoionic operating principle leads to versatile features of fast speed, lower power, non-volatility, simple device structure and high-density integration through crossbar array and three dimensional stacking.[3,4] In particular, the nanofilamentary conduction mechanism of the device allows superior scalability that can easily transcend the cutting-edge photolithography limitation,[5-9] endowing resistive switching memories with even multi-state quantized conductance (QC) characteristics and increased storage density, when the conductive filaments (CFs) elaborately shrink into atomic point contacts (APC).[10,11] Without the physical restriction imposed onto the miniaturization campaign nor the von Neumann communication bottleneck of the global semiconductor industry over the past half century,[1,12] quantized conductance also enables in-memory computing schemes which are powerful when dealing with data-intensive tasks in the artificial intelligence era.

In resistive switching devices, distribution and local rearrangement of the ionic species directly determine the evolution dynamics of conductive filaments, through which the transport of charge carriers regulates the device electrical performance.[13,14] When the switching parameters and consequently the lateral size of the conductive filament are precisely controlled, allowing electrons to pass ballistically through the one-dimensional constriction of APC without scattering, quantized conductance can be observed.[15,16] Therefore, deep insight and precise control of the nanoscale ionic procedure appear the most prominent requirements for practical resistive switching device applications.[17] Because ion migration inside the switching insulators is random in nature, the stochastic formation and evolution of multiple CFs usually result in severe deterioration of the device parameters, *viz.*,

fluctuated programming voltages and device resistances, limited endurance/retention and etc.[18-20] There are great efforts devoted to improving this situation. For instance, ion implantation or doping has been widely employed to regulate the concentration and distribution of mobile ions in the switching layer,[21-23] while the electrode engineering strategy with embedded nanopacticles is developed to confine the directional motion of mobile ion under the locally enhanced electric field.[24,25] Scanning probe microscope (SPM) provides a useful toolkit to correlate the sample local conductivity with ion migration and surface morphology in resistive switching memories.[26] Taking its ability of nanolithography patterning *via* local ion manipulation and surface electrochemistry into account,[27-29] the conductive mode of SPM technique (e.g. conductive-atomic force microscope) is also capable of accurately fabricating artificial nanostructure and electronic devices.[30,31] By directing the oriented migration of mobile ions with tip-enhanced local electric field, the scanning probe microscope may facilitate the controlled formation and evolution of conductive filaments, thereby significantly improving the overall performance of the memory devices.[32-35]

In this contribution, we for the first time report the controlled formation of atomic point contact in resistive switching devices, with the assist of scanning probe microscope. Upon inducing directional migration of oxygen anions with voltage-biased SPM tip, conical concaves can be formed at exact location of the hafnium oxide resistive switching layer with controlled dimensions. Capping the top electrode will generate inward protrusion into the hafnium oxide insulating layer, which could not only reduce the effective thickness of the switching matrix, but also confine the electric field to highly localized region with more oxygen vacancies. Single conductive filament and atomic point contact are consequently formed. As such, the integration density, energy-efficiency, stability and reliability of the memory device are all greatly improved. More importantly, we have successfully achieved continuous modulation of 16 half-integer multiples of quantized conductance states, which

might offer promising opportunity for developing high-performance storage and neuromorphic computing paradigm.

RESULTS AND DISCUSSION

Based on the filamentary conduction theory,[36,37] plural and percolative CFs are usually formed by random mobile ion migration along the grain boundaries in polycrystalline oxide films (**Figure 1a**). The stochastic annihilation and regeneration of the multiple CFs will result in severe fluctuation of the programming voltages and ON/OFF resistances, as well as the deterioration of device retention and endurance performance,[33,38] which appear critical obstacles that hinder the resistive switching memory for practical applications. The highly leaky pathways, associated with the abundant numbers of crystalline defects, would also lead to a large OFF state current and power consumption of the devices.[39,40] To restrain the random formation and evolution of the conductive filaments, herein we have deliberately utilized scanning probe microscope as a pre-treatment toolkit to regulate the ion and electric field distribution across the oxide switching layers, with the aim to produce single CF and APC in memory devices. As illustrated in **Figure 1b**, the voltage-biased SPM tip can act as a microelectrode when it is placed directly onto the amorphous HfO_x oxide thin films, confining the external electric field locally around the tip frontier and promoting the migration of the top layer oxygen anions toward the tip area.[41] The large current flowing through the tip and thus local high temperature may also facilitate in activating the oxygen vacancies for migration. Subsequent redox reaction leads to oxygen gas eruption from the interface, the accumulation of which will greatly modify the morphology of the oxygen-deficient region into a conical pit. Inverted cone-shape electrode is then obtained after depositing the top Pt layer.[42] Together with the reduced hafnium oxide layer thickness and the significantly increased oxygen vacancy concentration under the cone-shape electrode protrusion region, the local electrical field enhancement favors the exact formation of single conductive filament at the location of

the Pt projection. Eliminating the random generation and evolution of multiple conductive filaments, the overall device performance, the switching uniformity, stability and reliability in particular, are expected to be improved through this tip-assist electrode engineering strategy.

With the above hypothesis, hafnium oxide nanofilm was prepared directly on commercial Pt/Ti/SiO_2 substrate by radio-frequency magnetron sputtering technique. Amorphous HfO_x layer with the thickness of 10 nm, smooth surface topography with a root-mean-square roughness of 0.38 nm and the surface composition of $HfO_{1.6}$ is received by adjusting the RF power, sputtering time, deposition temperature and atmosphere (**Figures 2a**, **2b** and **S1**). In order to construct single conductive filament and atomic point contact inside the oxide switching layer, the sample was probed with a platinum SPM tip in contact mode to perform the electrochemical ion manipulation and *in-situ* morphology/conductivity measurements in ambient environment. Direct-current voltage sweeping was applied onto the tip with respect to the grounded bottom Pt electrode, which reproduced typical Pt/HfO_x/Pt device structure and operation of HfO_x-based resistive random access memory(RRAM) devices.[43] To facilitate the oxygen anions migration toward the SPM tip and their electrochemical reactions, voltage sweeps with various peak amplitudes and loading times were applied and assessed (**Figure S2**). Initially, the hafnium oxide layer shows relatively good insulating behavior, which allows the effective loading of electric field for mobile ion manipulation. Atomic Force Microscope (AFM) and Conductive-Atomic Force Microscope (C-AFM) graphs reveal that low voltage amplitudes cannot trigger any morphological or conductivity changes to the hafnium oxide nanofilm, while that exceeding 8 V can result in permanent breakdown of the insulating layer with drastic oxygen eruption. Therefore, the moderate bias voltage amplitude of 6 V was selected for the subsequent operations. Upon sweeping the HfO_x nanofilm at fixed position with the SPM tip between 0 V and 6 V for 5 times, the topography of the oxide layer begins to change (**Figure 2c**). Shallow dent with the depth < 1 nm can be observed with

simultaneous volatile resistive switching characteristics monitored at the same position (**Figure S3a**). The volatility of the current-voltage (I-V) curve can be ascribed to the small compliance current of 500 nA during each voltage sweep, which not only protects the sample from being permanently broken down but also limits the degree of oxygen ion migration and electrochemistry to form a transient CF. As the voltage sweeping continues and reaches 20 times, the downward conical pit becomes clearer with the depth increasing to ~ 1.6 nm (**Figure 2d** and **S3b**). Due to the irreversible accumulation of oxygen vacancies in the pit area, the electrical conductivity of the sample develops continuously. The I-V curve obtained at this stage does not coincide with that plotted in the right panel of **Figure 2c** anymore. After 50 sweeping cycles, the depth of the mature concave becomes 3.5 nm (**Figure 2e**) while the threshold switching voltage drops from 5.7 V to 1.9 V (**Figure 2f**). Accordingly, the shape and dimension of the conical pit could be controlled by deliberately tuning the peak amplitudes and loading times of the tip-voltage sweeps. Besides the modulation of local mobile ion concentration and distribution around the pit, the reduced film thickness may also account for the observed decreasing switching voltages. Being consistent with the tip-regulation strategy, only one conical concave was observed in the adjacent neighborhood upon applying 6 V voltage sweeps for 50 times (**Figure S3b**), suggesting that single inward electrode protrusion would be introduced into the switching matrix after capping the top platinum layer with electron beam evaporation (sample A). It is noteworthy that the hysteresis of the I-V curve shrinks as the voltage sweeping processes continues. Generally, as the thickness of the oxide layer decreases, smaller voltage is required to drive the migration of oxygen ions/vacancies to promote the device current to the compliance level. In the meanwhile, in thinner oxide layer with deeper pits, the concentration of oxygen vacancies is larger than that of the thicker oxide layer with shallower pits. This will also contribute to the smaller threshold switching voltage. On the other hand, as the oxygen vacancies concentration

increases, relatively stronger and more stable conductive filaments will be formed under the pit area and consequently reduces the hold voltage significantly. As an overall effect, the hysteresis in the I-V curve shrinks as shown in **Figure 2c** to **2e**.

For comparison purpose, control sample B with flat Pt/HfO_x interface and device parameter of 100 μm was also fabricated on the same 1×1 cm substrate. Both samples A and B were cut into transmission electron microscopic (TEM) specimens through focused ion beam (FIB) technique, and were observed under high resolution TEM accordingly. In order to visualize the electrode protrusion and sample composition more clearly, we increased the tip-treatment to 100 times so that the processed area shows more obvious structural and elemental changes. As such, the deeper pit and Pt protrusion can be distinguished easily from the hafnium oxide background. Being different from the featureless pattern of the untreated sample (**Figure 3a**), high resolution TEM and high-angle annular dark-field scanning transmission electron microscopy (HAADF STEM) images of the tip-treated sample show clearly that the top electrode extends into the HfO_x layer to form a cone-shaped inward protrusion (**Figure 3b** and **3c**). The diameter of the protrusion at its base is estimated to be ~ 20 nm while the height is ~ 6 nm as enclosed by the dotted blue line in **Figure 3b**, and the effective thickness of the underneath hafnium oxide is reduced to less than 4 nm. Energy dispersive spectroscopy (EDS) mappings of the platinum (L), hafnium (L) and oxygen (K) edges in the pitted region reveal that Pt has a good distribution coincidence with the top and bottom electrodes in HRTEM image (**Figures 3d-f**). Simultaneously, oxygen content in the pitted and underneath regions is much lower than that of the bulk HfO_x matrix (**Figure 3e**). As labeled in **Figure 3b**, positions 3 and 4 in the edge and center areas under the Pt protrusion show Hf/O atomic ratios of 1:0.7 and 1:0.4, respectively, as derived from the EDS results. It indicates a radial distribution of oxygen vacancies in the inward cone-shape concave, which can be ascribed to the tip-enhanced directional migration of oxygen anions under the locally

concentrated electric field. Short-distance movement of Hf species away from the pit area under the applied electric field may also contribute to the thinner oxide layer thickness and larger Hf/O atomic ratio after tip-treatment. In comparison, position 2 in the unaffected area of the HfO_x matrix carries identical microstructure and chemical composition (with the Hf/O atomic ratio of 1:1) as that of position 1 in the as-made hafnium oxide nanofilm of **Figure 3a**. It is noteworthy that the oxygen-deficient region has a diameter of around 8 nm, as enclosed by the dotted white line in **Figure 3e**, suggesting that ultra-scalable resistive switching devices with controlled growth of CF and high-density crossbar arrays can be achieved with the present SPM tip-assist strategy.[44,45] Interestingly, the hafnium species distribution frontier (although somehow overlapped with the Pt signals) also shows an downward cone shape as sketched in **Figure 3f**, indicating that Hf^{2+} cations undergo synchronous migration with oxygen in the opposite direction.[46]

Due to the presence of abundant ion migrating defects in the as-fabricated amorphous hafnium oxide nanofilms, multiple CFs with branched geometry can be formed and evolve randomly, giving rise to large discrepancy in the switching voltages and ON/OFF resistances, as well as substantial device degradation that leads to cycle-to-cycle and device-to-device variation and limited endurance performance of the memory.[47,48] In **Figures 4a** and **4b**, the Pt/HfO_x/Pt device with flat hafnium oxide-platinum interface exhibits bipolar resistive switching behavior in the current-voltage curves, with a large forming voltage of ~ 6.0 V and significant fluctuation in the programming voltages. The set voltages range from 2.5 V to 0.9 V, while the reset voltages vary between -0.6 V and -0.9 V, respectively. During electrical measurements, the bottom electrode was always grounded while the DC sweeping voltages were applied to the top electrode. The dispersion coefficients are 23% and 18% for the set and reset voltages. With the presence of competition between a plurality of conductive filaments, resistive switching may not occur exactly at the same position for each time. The unregulated

electric field across the switching matrix may result in simultaneous radial and longitudinal migration of mobile ions, giving rise to the coexistence of both sharp and gradual switching behaviors during the reset processes.[49,50] The ON/OFF resistances also fluctuate from cycle to cycle in the same device. When a localized oxygen-deficient channel is preferentially formed by SPM tip pre-treatment (50 cycles) and electrode protrusion capping, single CF could be generated in a controllable manner in the switching matrix. As such, the forming voltage decreases to 2.2 V (**Figure 4b** and **4c**), primarily due to the reduced film thickness, greatly increased oxygen vacancy concentration, as well as the locally concentrated and enhanced electric field under the cone shape electrode extending into the hafnium oxide nanofilm. Control samples with flat HfO_x/Pt interfaces and 6~10 nm hafnium oxide film thickness also exhibit relatively large and obviously varied programming voltages (**Figure S4**). Therefore, one can conclude that the regulation in oxygen vacancy concentration and local electric field may greatly influence the switching characteristics of the memory devices. Comparing **Figures 4a** and **4c**, the current-voltage switching curves become more uniform with the controlled formation and evolution of a single CF in the hafnium oxide layer. The redistribution of oxygen vacancies and the local electric field enhancement under the Pt electrode protrusion can confine the migration and electrochemistry of the oxygen anions in a relatively narrower region, so that the possibility would be reduced for the multiple conductive filaments formation and their subsequent competition during evolution. Repeated disruption and regeneration at the exact same conductive filament can suppress the variation in the switching voltages and ON/OFF resistances significantly (**Figure 4b** and **4d**), and the device shows promising retention and endurance characteristics (**Figure S5**). The cycle-to-cycle dispersion coefficients have been reduced for at least 33% for the programming voltages and device resistances in the ON/OFF states, meanwhile the device-to-device variations in the switching parameters are also improved by using the tip-modulated electrode engineering

approach (**Figures 4e** and **4f**). Nevertheless, several intermediate steps or smooth current changes can be observed in the negatively biased reset process of **Figure 4a** and **4c**, which offer the possibility of continuously modifying the dimension of the conductive filaments and accessing of the quantum (atomic) point contact as the CFs shrink down.

Over the past decade, several approaches employing "edge effects" have been developed to improve the switching uniformity and reliability of RRAM devices. For instance, Liu and coworkers embedded nanoparticles in the switching matrix to regulate its microstructure and distribution of the internal electric field,[5,51,52] whereas Ryoo et al used staggered active layers to achieve the same target.[53,54] Although the resultant devices show enhanced performance in comparison with that of the controlled samples, there are still rooms for further optimization since the placement of the nanoparticles nor the wrinkle patterns of the staggered layers cannot be controlled exactly during thin film deposition. Multiple nanoscale conductive filaments may be formed throughout the entire device area with the typical size of 100 nm to 10 μm, the random evolution of which can still lead to deteriorated switching uniformity. Adopting intensive photolithographic fabrication may define arbitrary pattern onto the device to confine local electric field for single filament formation,[55,56] nevertheless it is less favored in terms of cost and convenience concerns. For instance, the dimension of the concave pit formed by nano-indentation is generally pre-defined by the size of the mechanical mold. Relatively, the present SPM-assisted approach offers a simple yet effect alternative for performance modulation of oxide based resistive switching devices, with controlled formation and evolution of single pseudo-straight conductive filament under the tip or concave area, which can be achieved by adjusting the biased voltage applied through the tip that can modify both the geometry and mobile ions/vacancies profiles of the oxide thin film.

The dimension of the oxygen vacancy based CF can be potential scaled down to 8 nm by SPM pre-treatment (**Figure 3e**), and is predicted to be even as small as 0.4 nm in HfO_x

switching matrix according to the reference.[57-59] This not only allows the production of ultra-small memory and its high-density integration into large crossbar array or three dimensional stacks, but also enables the possibility of quantized conductance feature as the diameter of the charge carrier transport channel shrinks to that comparable to the Fermi wavelength or even smaller than the mean free path of the electrons. Ballistic charge carrier transport through the quasi-one-dimensional system without scattering gives rise to the development of device conductance in the unit of $G_0=2e^2/h$ based on Landau transmission theory,[60,61] where e is the elemental charge of electron, h is the Planck's constant and G_0=77.5 μS.[62-65] However, conductance quantization behavior is not always exactly observed in resistive switching memories, as the presence of multiple CFs usually leads to a summarized (fractional) conductance value and thus missing of certain QC states (**Figure S6**).[66,67] With these concerns, the fine-tuning of single conductive filament into atomic point contact with SPM pre-treatment will promise a better control of the quantized conductance in terms of the accessibility, stability and reliability.[68,69] In the Pt/HfO_x/Pt device with inward conical Pt electrode protrusion, it was observed that gradual neutralizing of the CF observed in the negatively-biased resetting process can result in a stepwise change of the current-voltage characteristics (**Figure S7**). Through consecutively increasing the stopping voltage during negative sweeps, continuous modulation of device conductance was realized with the active diameter of 100 μm in ambient environment (**Figure 5a**). The conductance value shows a strong linear dependence on the stop voltage amplitude (**Figure 5b**), which satisfies the basic requirements for neuromorphic computation using resistive switching devices.[70,71] In cumulative histogram which is based on approximately 800 reset traces (with the corresponding conductance values recorded at 0.02 V), conductance peaks are observed and primarily located at the half-integer multiples of G_0 in the range of $0.5G_0$ to $8G_0$ (**Figure 5c**), producing at least 16 quantized state for 4-bit binary operation and even decimal algorithm.

The existence of half-integer multiples of G_0can be either arising from the chemical potential difference of the electrodes or related to the absence of spin degeneracy associated with the weak magnetism in oxygen vacancy defects.[68,72,73] Fractional conductance variation was also observed between $8G_0$ and $10G_0$, which may be ascribed to the non-negligible carrier scattering when the channel dimension becomes larger. Tuning efficiency in device conductance is further assessed by applying successive voltage ramps with increasing stop voltages during the reset process. When a group of incremental sweep voltages is applied from 1.0 V to 1.16 V with the step of 0.04 V, all the integer multiples of G_0 in QC range of $1G_0$ to $5G_0$have been reproduced repeatedly (**Figure 5d**). The retention of these quantized conductance states are more than 10^4 s at room temperature as shown in **Figure 5e**, again indicating that the SPM tip-enhanced approach provides a promising and universal way of optimizing the resistive switching and conductance quantization in oxide memory device for multi-value storage and in-memory computation applications.

CONCLUSIONS

To summarize, we developed a universal tip-enhanced approach for performance modulation of oxide based resistive switching devices. By using the voltage-biased scanning probe microscope tip as a microelectrode to regulate the directional migration of oxygen anions inside the hafnium oxide nanofilm, the morphology and mobile ion distribution of the switching matrix can be changed significantly. The formation of conical concave with controlled dimension not only reduces the thickness of the oxide layer, but also allows the formation of metal protrusion from top electrode into the HfO_x nanofilm. Together with the increasing of local concentration of oxygen vacancy in the underneath region, the centralization and enhancement of local electric field consequently result in the nucleation and growth of single conductive filament, so that the integration density, stability and reliability are greatly improved for the memory device. 16 half-integer multiples of quantized conductance states has been realized through single atomic point contacts induced by deliberate tuning of the filament dimension in the resistive switching device, which might be used for multilevel data storage and high order neuromorphic computing paradigm.

METHODS

Sample Preparation: The Pt/HfO_x/Pt devices were fabricated on commercial SiO_2/Ti/Pt wafers (1 cm×1 cm), by depositing the 10 nm HfO_x nanofilm through RF magnetron sputtering technique in a pure argon environment with the environmental pressure of 1 Pa and using high purity HfO_2 ceramic (99.995%) as the target. For samples with flat HfO_x/Pt interface, the top platinum electrodes with the thickness of 50 nm were directly deposited onto the HfO_x nanofilm by electron beam evaporation at a pressure of ~10^{-6} Pa and a deposition rate of ~0.5 Å/s at room temperature. For samples with inward conical Pt electrode protrusion, a layer of photoresist (AZ-5214E) was first spin-coated onto the HfO_x nanofilm, followed by photolithography patterning using a positive photomask and lift-off process to define an exposed HfO_x area with the radii of 100 μm. Then a scanning probe microscope tip was placed onto surface of the circular HfO_x exposed area in contact mode, with which local voltage sweeps with different amplitudes and loading cycles were applied onto the sample. During operation the bottom Pt electrode was always grounded and all the operations were conducted in ambient environment. Afterwards, Pt top electrodes were deposited into the circular pattern through E-beam evaporation.

Characterization: The microstructure of the as-deposited HfO_x nanofilms was investigated by X-ray diffractive (XRD) analysis (Bruker AXS, D8 Discover) using Cu-K_α radiation. X-ray photoelectron spectroscopic analysis (XPS, SHIMADZU, AXIS ULTRA DLD) of the HfO_xlayer was performed to investigate the film composition. A monochromatic Al-K_α X-ray source (1486.6 eV photons) was used at a constant dwell time of 100 ms. A pass energy of 80 eV or 40 eV was employed for the wide and core-level spectra scan, respectively. The X-ray source was run at a reduced power of 150 W (15 kV and 10 mA). The pressure in the analysis chamber was maintained at 10^{-8} Torr or lower during each measurement. The core-level signals were recorded at a photoelectron take-off angle (α, measured with respect to the

sample surface) of 90°. All binding energies were referenced to the C 1s hydrocarbon peak at 284.6 eV. Surface elemental stoichiometries were determined from XPS spectral area ratios and they were reliable within ±5 %. The elemental sensitivity factors were calibrated using stable binary compounds of well established stoichiometries. Background correction and peak fit features were performed to the data using CASA XPS software. Cross-sectional HRTEM and scanning transmission electron microscope (STEM) images with EDS of the samples were recorded on a FEI Titan Themis 200 transmission electron microscope by SAE Magnetics (H.K.) Ltd. Spatial resolutions are 0.1 nm and 0.08 nm for HRTEM and STEM. The TEM specimens were prepared on a FEI Helios 450S dual beam focus ion beam (FIB) workstation with the dimension of 500 nm height × 3 μm width × 40 nm thickness. Scanning probe microscope (Veeco Dimension 3100V) was used for tip-assisted sample preparation, as well as AFM morphology and C-AFM local conductivity measurements of the HfO_x layer. Electrical characteristics of the devices were recorded using an Agilent B1500A semiconductor parameter analyzer. The biased voltages were applied onto the Pt top electrode, meanwhile the Pt bottom electrode was grounded as a reference.

ASSOCIATED CONTENT

Supporting Information.

The following files are available free of charge.

X-ray diffractive (XRD) and X-ray photoelectron spectra (XPS) patterns, morphology and conductivity mapping in C-AFM mode, resistive switching characteristics diagram, retention and endurance performance diagram, histogram of the device conductance.

AUTHOR INFORMATION

Corresponding Author

*gang.liu@sjtu.edu.cn

*zhengxuejun@xtu.edu.cn

*runweili@nimte.ac.cn

Notes

The authors declare no competing financial interest.

ACKNOWLEDGMENT

This work was supported by the National Natural Science Foundation of China (61722407, 11832016, 51775471, 61704178, 61674153 and 51525103), National Key R&D Program of China (2017YFB0405600 and 2017YFF0105000), Program for Changjiang Scholars, Provincial Natural Science Foundation of Hunan (2018JJ4037) and Innovative Research Team in University (IRT-14R48).

REFERENCES

[1] Waldrop, M. M. The chips are down for Moore's law. *Nature News* **2016**, 530, 144-148.

[2] Schaller, R. R. Moore's law: past, present and future. *IEEE Spectrum* **1997**, 34, 52-59.

[3] Pan, F.; Gao, S.; Chen, C.; Song, C.; Zeng, F. Recent progress in resistive random access memories: materials, switching mechanisms, and performance. *Mater. Sci. Eng. R*. **2014**, 83, 1-59 .

[4] Seok, J. Y.; Song, S.-J.; Yoon, J. H.; Yoon, K. J.; Park, T. H.; Kwon, D. E.; Lim, H. K.; Kim, Gun H.; Jeong, D. S.; Hwang, C. S. A review of three-dimensional resistive switching cross-bar array memories from the integration and materials property points of view. *Adv. Funct. Mater*. **2014**, 24, 5316-5339.

[5] Liu, Q.; Long, S.; Lv, H.; Wang, W.; Niu, J.; Huo Z.; J. Chen; Liu, M. Controllable growth of nanoscale conductive filaments in solid-electrolyte-based ReRAM by using a metal nanocrystal covered bottom electrode. *ACS Nano* **2010**, 4, 6162-6168.

[6] Chen, J. Y.; Huang, C. W.; Chiu, C. H.; Huang, Y. T.; Wu, W. W. Switching kinetic of VCM-based memristor: evolution and positioning of nanofilament. *Adv. Mater.* **2015**, 27, 5028-5033.

[7] Kim, H. J.; Park, T. H.; Yoon, K. J.; Seong, W. M.; Yoon, J. H.; Hwang, C. S. Fabrication of a Cu-cone-shaped cation source inserted conductive bridge random access memory and its improved switching reliability. *Adv. Funct. Mater.* **2019**, 29, 1806278.

[8] Celano, U.; Fantini, A.; Degraeve, R.; Jurczak, M.; Goux, L.; Vandervorst, W. Scalability of valence change memory: From devices to tip-induced filaments. *AIP Adv.* **2016**, 6, 085009.

[9] Govoreanu, B.; Kar, G. S.; Chen Y. Y.; Goux, L.; Wouters, D. J. 10× 10nm^2 Hf/HfO_x crossbar resistive RAM with excellent performance, reliability and low-energy operation. *2011 International Electron Devices Meeting IEEE* **2011**, 3161-3164.

[10] Jang, M. H.; Agarwal, R.; Nukala, P.; Choi, D.; Johnson, A. T. C.; Chen, I. W.; Agarwal, R. Observing oxygen vacancy driven electroforming in Pt-TiO_2-Pt Device *via* strong metal support interaction. *Nano Lett*. **2016**, 16, 2139-2144.

[11] Zhu, X. J.; Shang, J.; Liu, G.; Li, R.-W. Ion transport-related resistive switching in film sandwich structures. *Chin. Sci. Bull*. **2014**, 59, 2363-2382.

[12] Nandakumar, S. R.; Minvielle, M.; Nagar, S.; Dubourdieu, C. A 250 mV Cu/SiO_2/W memristor with half-Integer quantum conductance states. *Nano Lett.* **2016**, 16, 1602-1608.

[13] Hong, D.-S.; Chen, Y.-S.; Li, Y.; Yang, H.-W.; Wei, L.-L.; Shen, B.-G.; Sun, J.-R. Evolution of conduction channel and its effect on resistance switching for Au-WO_{3-x}-Au devices. *Sci. Rep*. **2014**, 4, 4058.

[14] Sharath, S. U.; Vogel, S.; Luna, L. M.; Hildebrandt, V. S, E. Control of switching modes and conductance quantization in oxygen engineered HfO_x based memristive devices. *Adv. Funct. Mater*. **2017**, 27, 1700432.

[15] Smith, D. P. E. Quantum point contact switches. *Science* **1995**, 269, 371-373.

[16] Agraït, N. Quantum properties of atomic-sized conductors. *Phys. Rep.* **2003**, 377, 81-279.

[17] Lee, J.; Lu, W.-D. On-demand reconfiguration of nanomaterials: when electronics meets ionics. *Adv. Mater.* **2018**, 30, 1702770.

[18] Fang, Y.; Yu, Z.; Wang, Z.; Zhang, T.; Yang, Y.; Cai, Y.; Huang, R. Improvement of HfO_x-based RRAM device variation by inserting ALD TiN buffer layer. *IEEE Electron. Dev. Lett*. **2018**, 39, 819-822.

[19] Wu, Q.; Banerjee, W.; Cao, J.; Ji, Z.; Li, L.; Liu, M. Improvement of durability and switching speed by incorporating nanocrystals in the HfO_x based resistive random access memory devices. *Appl. Phys. Lett.* **2018**, 113, 023105.

[20] Hou, Y.; Celano, U.; Goux, L.; Liu, L.; Degraeve, R.; Cheng, Y.; Vandervorst, W. Multimode resistive switching in nanoscale hafnium oxide stack as studied by atomic force microscopy. *Appl. Phy. Lett.* **2016**, 109, 023508.

[21] Schindler, C.; Thermadam, S. C. P.; Waser, R.; Kozicki, M. N. Bipolar and unipolar resistive switching in Cu-doped SiO_2. *IEEE Trans. Electron. Dev.* **2007**, 54, 2762-2768.

[22] Guan, W.; Long, S.; Liu, Q.; Liu, M.; Wang, W. Nonpolar nonvolatile resistive switching in Cu doped ZrO_2. *IEEE Electron. Dev. Lett.* **2008**, 29, 434-437.

[23] Muenstermann, R.; Menke, T.; Dittmann, R.; Waser, R. Coexistence of filamentary and homogeneous resistive switching in Fe-Doped $SrTiO_3$ thin-film memristive devices. *Adv. Mater.* **2010**, 22, 4819-4822.

[24] You, B.-K.; Kim, J. M.; Joe, D. J.; Yang, K.; Shin, Y. G.; Jung, Y. S.; Lee, K. J. Reliable memristive switching memory devices enabled by densely packed silver nanocone arrays as electric-field concentrators. *ACS Nano* **2016**, 10, 9478-9488.

[25] Ling, H.; Yi, M.; Nagai, M.; Xie, L.-H.; Wang, L.-Y.; Hu, B.; Huang, W. Controllable organic resistive switching achieved by one-step integration of cone-shaped contact. *Adv. Mater.* **2017**, 29, 1701333.

[26] Zhang, J.; Chen, P, Yuan, B. K.; Ji, W.; Cheng, Z. H.; Qiu, X. H. Real-space identification of intermolecular bonding with atomic force microscopy. *Science* **2013**, 342, 611-614.

[27] Li, R.-W.; Kanki, T.; Tohyama, H. A.; Hirooka, M.; Tanaka, H.; Kawai, T. Nanopatterning of perovskite manganite thin films by atomic force microscope lithography. *Nanotechnology* **2004**, 16, 28-31.

[28] Suzuki, N.; Tanaka, H.; Kawai, T. Epitaxial transition metal oxide nanostructures fabricated by a combination of AFM lithography and molybdenum lift-off. *Adv. Mater*. **2008**, 20, 909-913.

[29] Goto, K.; Tanaka, H.; Kawai, T. Controlled fabrication of epitaxial $(Fe,Mn)_3O_4$ artificial nanowire structures and their electric and magnetic properties. *Nano Lett.* **2009**, 9, 1962-1966.

[30] Ge, J.; Chaker, M. Oxygen vacancies control transition of resistive switching mode in single-crystal TiO_2 memory device. *ACS Appl. Mater. Interfaces* **2017**, 9, 16327-16334.

[31] Zhu, X.-J.; Su, W.-J.; Liu, Y.-W.; Hu, B.-L.; Pan, L.; Lu, W.; Zhang, J.-D.; Li, R.-W. Observation of conductance quantization in oxide-based resistive switching memory. *Adv. Mater.* **2012**, 24, 3941-3946.

[32] Midya, R.; Wang, Z.; Zhang, J. Anatomy of Ag/Hafnia-based selectors with 10^{10} nonlinearity. *Adv. Mater*. **2017**, 29, 1604457.

[33] Kravets, V. G.; Marshall, O. P.; Schedin, F. Plasmon-induced nanoscale quantised conductance filaments. *Sci. Rep*. **2017**, 7, 2878-2887.

[34] Celano, U. Metrology and physical mechanisms in new generation ionic devices. Springer, **2016**, pp 87-111

[35] Miao, F.; Strachan, J. P.; Yang, J. J.; Zhang, M.-X.; Goldfarb, I.; Torrezan, A. C.; Williams, R. S. Anatomy of a nanoscale conduction channel reveals the mechanism of a high-performance memristor. *Adv. Mater.* **2011**, 23, 5633–5640.

[36] Park, G. S.; Li, X. -S.; Kim, D. C.; Jung, R. J.; Lee, M. J.; Seo, S. Observation of electric-field induced Ni filament channels in polycrystalline NiO_x film. *Appl. Phys. Lett.* **2007**, 91, 222103.

[37] Lanza, M.; Bersuker, G.; Porti, M.; Miranda, E.; Nafría, M.; Aymerich, X. Resistive switching in hafnium dioxide layers: Local phenomenon at grain boundaries. *Appl. Phys. Lett.* **2012**, 101, 193502.

[38] Chen, C.; Gao, S.; Zeng, F.; Wang, G.-Y. Conductance quantization in oxygen-anion-migration-based resistive switching memory devices. *Appl. Phys. Lett.* **2013**, 103, 043510.

[39] Woo, H.; Vishwanath, S. K.; Jeon, S. Excellent resistive switching performance of Cu-Se-based atomic switch using lanthanide metal nanolayer at the Cu-Se/Al_2O_3 interface. *ACS Appl. Mater. Interfaces* **2018**, 10, 8124-8131.

[40] Wang, X.-F.; Tian, H.; Zhao, H.-M.; Zhang, T.-Y.; Mao, W.-Q.; Qiao, Y.-C.; Pang, Y.; Li, Y.-X.; Yang, Y.; Ren, T.-L. Interface engineering with MoS_2-Pd nanoparticles hybrid structure for a low voltage resistive switching memory. *Small* **2018**, 14, 1702525.

[41] Yang, Y.; Zhang, X.; Qin, L.; Huang, R. Probing nanoscale oxygen ion motion in memristive systems. *Nat. Commun.* **2017**, 8, 15173.

[42] Niu, G.; Calka, P.; Maur, M. A. D.; Calka, P.; Santoni, F. Geometric conductive filament confinement by nanotips for resistive switching of HfO_2-RRAM devices with high performance. *Sci. Rep*. **2016**, 6, 25757.

[43] Zidan, M. A.; Strachan, J. P.; Lu, W.-D. The future of electronics based on memristive systems. *Nat. Electron*. **2018**, 1, 22-29.

[44] Celano, U.; Goux, L.; Degraeve, R.; Fantini, A.; Richard, O.; Bender, H.; Vandervorst, W. Imaging the three-dimensional conductive channel in filamentary-based oxide resistive switching memory. *Nano Lett.* **2015**, 15, 7970–7975.

[45] Park, G. S.; Kim, Y. B.; Park, S. Y.; Li, X. S.; Heo, S.; Lee, M.-J.; Kim, K. *In situ* observation of filamentary conducting channels in an asymmetric Ta_2O_{5-x}/TaO_{2-x} bilayer structure. *Nat. Commun.* **2013**, 4, 2382.

[46] Schie, M.; Müller, M. P.; Salinga, M.; Waser, R.; De Souza, R. A. Ion migration in crystalline and amorphous HfO_x. *J. Mater. Chem. C* **2017**, 146, 094508.

[47] Shang, J.; Xue, W.-H.; Ji, Z.-H.; Liu, G.; Niu, X.-H.; Yi, X.-H.; Pan, L.; Zhan, Q.-F.; Xu, X.-H.; Li, R.-W. Highly flexible resistive switching memory based on amorphous-nanocrystalline hafnium oxide films. *Nanoscale* **2017**, 9, 7037-7046.

[48] Pan, L.; Ji, Z.-H.; Yi, X.-H.; Zhu, X.-J.; Chen, X.-X.; Shang, J.; Liu, G.; Li, R.-W. Metal-organic framework nanofilm for mechanically flexible information storage applications. *Adv. Funct. Mater.* **2015**, 25, 2677-2685.

[49] Zhao, X.; Ma, J.; Xiao, X. Breaking the current-retention dilemma in cation-based resistive switching devices utilizing graphene with controlled defects. *Adv. Mater*. **2018**, 30, 1705193.

[50] Miranda, E. A.; Walczyk, C.; Wenger, C.; Schroeder, T. Model for the resistive switching effect in HfO_2 MIM structures based on the transmission properties of narrow constrictions. *IEEE Electron. Dev. Lett.* **2010**, 31, 609-611.

[51] Wang, Z.-Q.; Xu, H.-Y.; Zhang, L.; Li, X. H.; Ma, J. G.; Zhang, X. T.; Liu, Y. C. Performance improvement of resistive switching memory achieved by enhancing local-electric-field near electromigrated Ag-nanoclusters. *Nanoscale* **2013**, *5*, 4490-4494.

[52] Bousoulas, P.; Stathopoulos, S.; Tsialoukis, D.; Tsoukalas, D. Low-power and highly uniform 3-b multilevel switching in forming free TiO_{2-x}-based RRAM with embedded Pt nanocrystals. *IEEE Electron. Dev. Lett.* **2016**, 37, 874-877.

[53] Ryoo, K.-C.; Kim, S.; Oh, J.-H.; Jung, S.; Jeong, H.; Park, B.-G. Novel protruded-shape unipolar resistive random access memory structure for improving switching uniformity through excellent conductive filament controllability. *Jpn. J. Appl. Phys.* **2012**, 51, 06FE06.

[54] Chuang, K.-C.; Lin, K.-Y.; Luo, J.-D.; Li, W.-S.; Li, Y.-S.; Chu, C.-Y.; Cheng, H.-C. Effects of electric fields on the switching properties improvements of RRAM device with a field-enhanced elevated-film-stack structure. *IEEE J. Electron. Dev. Soc.* **2018**, 6, 622-626.

[55] Niu, G.; Calka, P.; der Maur, M. A.; Santoni, F.; Guha, S.; Fraschke, M.; Hamoumou, P.; Gautier, B.; Perez, E.; Walczyk, C.; Wenger, C.; Carlo, A. D.; Alff, L.; Schroeder, T. Geometric conductive filament confinement by nanotips for resistive switching of HfO_2-RRAM devices with high performance. *Sci. Reps.* **2016**, 6, 25757.

[56] Sun, Y.; Song, C.; Yin, J.; Chen, X.; Wan, Q.; Zeng, F.; Pan, F. Guiding the growth of a conductive filament by nanoindentation to improve resistive switching. *ACS Appl. Mater. Interfaces* **2017**, 9, 34064-34070.

[57] Xue, K. H.; Miao, X. S. Oxygen vacancy chain and conductive filament formation in hafnia. *J. Appl. Phys*. **2018**, 123, 161505.

[58] Li, C.; Gao, B.; Yao, Y.; Guan, X. X.; Shen, X.; Wang, Y. G.; Huang, P.; Liu, L.-F.; Liu, X.-Y.; Li, J.-J.; Gu, C.-Z.; Kang, J.-F.; Yu, R.-C. Direct observations of nanofilament

evolution in switching processes in HfO_2-based resistive random access memory by in situ TEM studies. *Adv. Mater.* **2017**, 29, 1602976.

[59] Pi, S.; Li, C.; Jiang, H.; Xia, W.; Xin, H.; Yang, J. J.; Xia, Q. Memristor crossbar arrays with 6-nm half-pitch and 2-nm critical dimension. *Nat. Nanotechnol.* **2018**, 14, 35-39.

[60] Long, S.; Lian, X.; Cagli, C.; Cartoixà, X.; Rurali, R.; Miranda, E.; Jiménez, D.; Perniola, L.; Liu, M.; Suñé, J.Quantum-size effects in hafnium-oxide resistive switching. *Appl. Phys. Lett.* **2013**, 102, 183505.

[61] Li, Y.; Long, S.; Liu, Y.; Hu, C.; Teng, J.; Liu, Q.; Lv, H.; Suñé, J.; Liu, M. Conductance quantization in resistive random access memory. *Nanoscale Res. Lett.* **2015**, 10, 420-429.

[62] Yang, J. J.; Strukov, D. B.; Stewart, D. R. Memristive devices for computing. *Nat. Nanotechnol.* **2013**, 8, 13-24.

[63] Gao, S.; Yi, X.; Shang, J.; Liu, G.; Li, R.-W. Organic and hybrid resistive switching materials and devices. *Chem. Soc. Rev.* **2018**, 48, 1531-1565.

[64] Lian, X.; Cartoixa, X.; Miranda, E.; Suñé, J. Multi-scale quantum point contact model for filamentary conduction in resistive random access memories devices. *J. Appl. Phys.* **2014**, 115, 244507.

[65] Lv, H.; Xu, X.; Sun, P.; Liu, M. Atomic view of filament growth in electrochemical memristive elements. *Sci. Rep*. **2015**, 5, 13311.

[66] Sun, Y.; Wen, D. Ion-molecule complex dissociation and formation dynamics in LiCl aqueous solutions from 2D IR spectroscopy. *J. Phys. Chem. C* **2018**, 122, 10582-10592.

[67] Lee, M. J.; Park, G. S.; Seo, D. H.; Kwon, S. M.; Jun, H.; Kim, J. S. Reliable multivalued conductance states in TaO_x memristors through oxygen plasma-assisted electrode deposition with *in situ*-biased conductance state transmission electron microscopy analysis. *ACS Appl. Mater. Interfaces* **2018**, 10, 29757-29765.

[68] Mehonic, A.; Vrajitoarea, A.; Cueff, S.; Hudziak, S.; Howe, H.; Labbe, C.; Rizk, R.; Pepper, M.; Kenyon, A. J. Quantum conductance in silicon oxide resistive memory devices. *Sci. Rep*. **2013**, 3, 2708-2815.

[69] Terabe, K.; Hasegawa, T.; Nakayama, T.; Aono, M. Quantized conductance atomic switch. *Nature* **2005**, 433, 47-50.

[70] Krishnan, K.; Muruganathan, M.; Tsuruoka, T.; Mizuta, H.; Aono, M. Highly reproducible and regulated conductance quantization in a polymer-based atomic switch.

Adv. Funct. Mater. **2017**, 27, 1605104.

Captions for Figures

Figure 1. Schematic illustration for the construction of Pt/HfO_x/Pt resistive switching memory devices with (a) flat HfO_x/Pt and (b) inward conical Pt electrode protrusion, respectively.

Figure 2. (a) Atomic force microscopic topography and (b) cross-sectional transmission electron microscope images of the HfO_x nanofilm deposited on the Pt substrate. (c-e) Two dimensional topography (left panel), three dimensional topography (middle panel) and local current-voltage characteristics (right panel) of the as-deposited HfO_x nanofilm after being subjected direct-current conductive atomic force microscope sweeps with the amplitude of 6 V for 5, 20 and 50 times, respectively. (f) Evolution of the local threshold switching voltage with respect to the total numbers of the applied conductive atomic force microscopic sweeps.

Figure 3. High resolution transmission electron microscope images of the Pt/HfO_x/Pt resistive switching devices with (a) flat HfO_x/Pt interface and (b) inward conical Pt electrode protrusion, respectively. (c) Scanning transmission electron microscope image and (d-f) energy-dispersive spectroscopy mapping of the Pt (L), O (K) and Hf (L) edges of the device with cone-shaped Pt electrode protrusion, respectively.

Figure 4. (a) Resistive switching characteristics of the Pt/HfO_x/Pt device with flat HfO_x/Pt interface. (b) Forming characteristics and voltage distribution of Pt/HfO_x/Pt devices with different geometries and hafnium oxide thickness. Sample A is the device with inward conical Pt electrode protrusion and hafnium oxide thicknesses of 10 nm. Samples B to D are devices with flat HfO_x/Pt interface but different hafnium oxide thicknesses of 6 nm, 8 nm and 10 nm, respectively. (c) Resistive switching characteristics of the Pt/HfO_x/Pt device with inward conical Pt electrode protrusion. (d) Cumulative probability of the ON/OFF resistances over 200 cycles, device-to-device variation of the (e) switching voltages and (f) ON/OFF resistances of the Pt/HfO_x/Pt device with flat HfO_x/Pt interface and inward conical Pt electrode protrusion, respectively.

Figure 5. (a) Current-voltage characteristics of the Pt/HfO_x/Pt device with inward cone Pt electrode protrusion showing continuous modulation of device conductance. (b) Evolution of the device quantized conductance and the applied sweeping voltage maximum as a function of the sweeping cycles. (c) Histogram of the device quantized conductance obtained from ~ 800 reset processes. (d) Cyclic tolerance of quantized conductance between $1G_0$ and $5G_0$. (e) Room-temperature retention performance of the quantized conductance states.

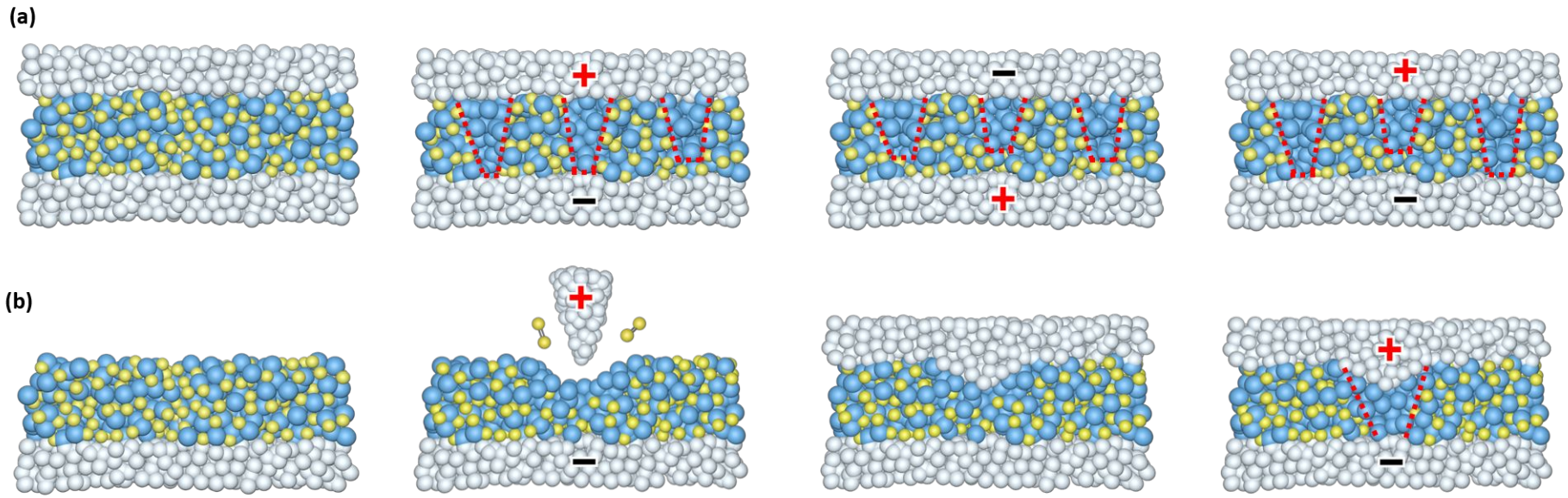

Figure 1. Schematic illustration for the construction of Pt/HfO_x/Pt resistive switching memory devices with (a) flat HfO_x/Pt and (b) inward conical Pt electrode protrusion, respectively.

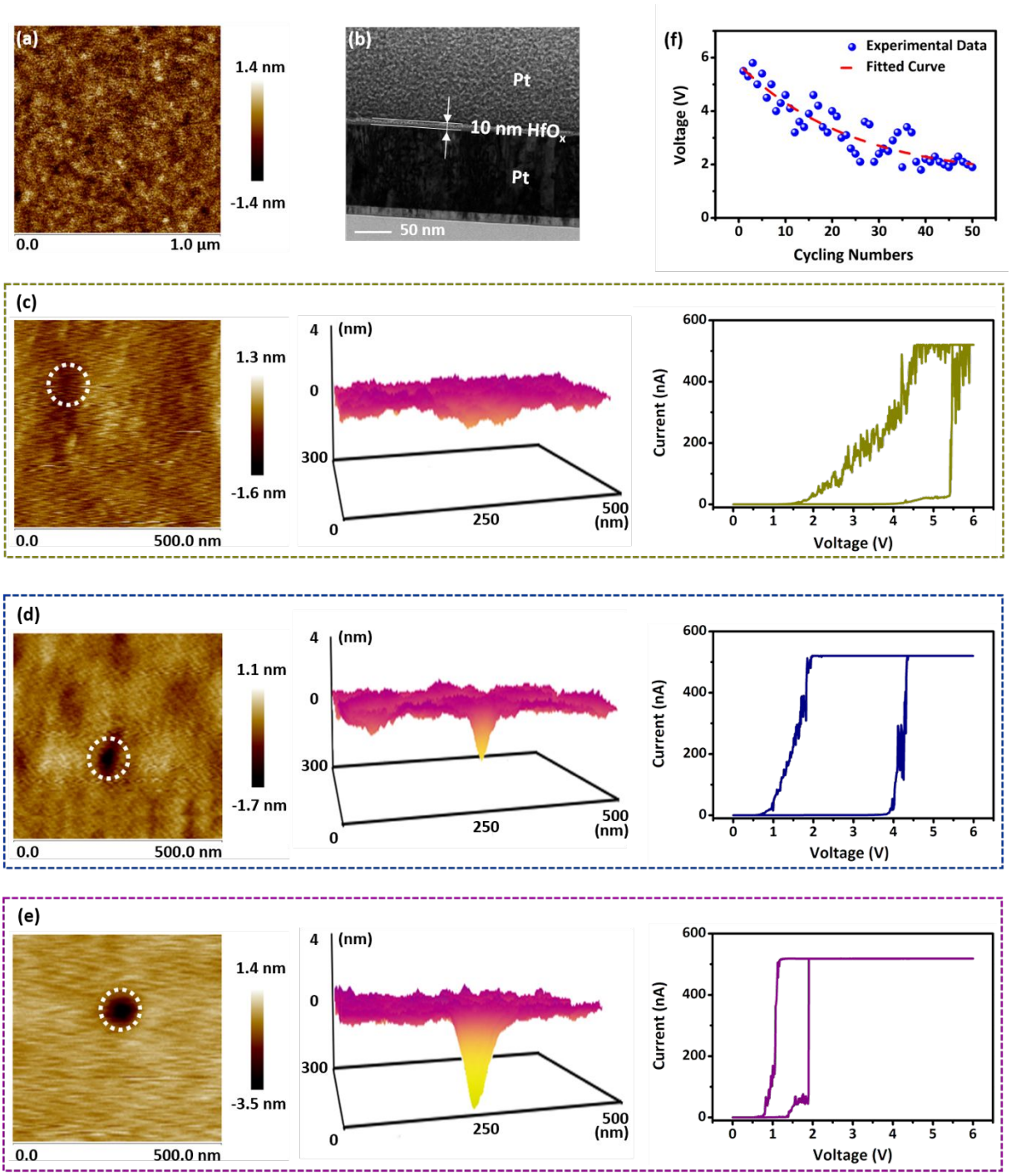

Figure 2. (a) Atomic force microscopic topography and (b) cross-sectional transmission electron microscope images of the HfO_x nanofilm deposited on the Pt substrate. (c-e) Two dimensional topography (left panel), three dimensional topography (middle panel) and local current-voltage characteristics (right panel) of the as-deposited HfO_x nanofilm after being subjected direct-current conductive atomic force microscope sweeps with the amplitude of 6 V for 5, 20 and 50 times, respectively. (f) Evolution of the local threshold switching voltage with respect to the total numbers of the applied conductive atomic force microscopic sweeps.

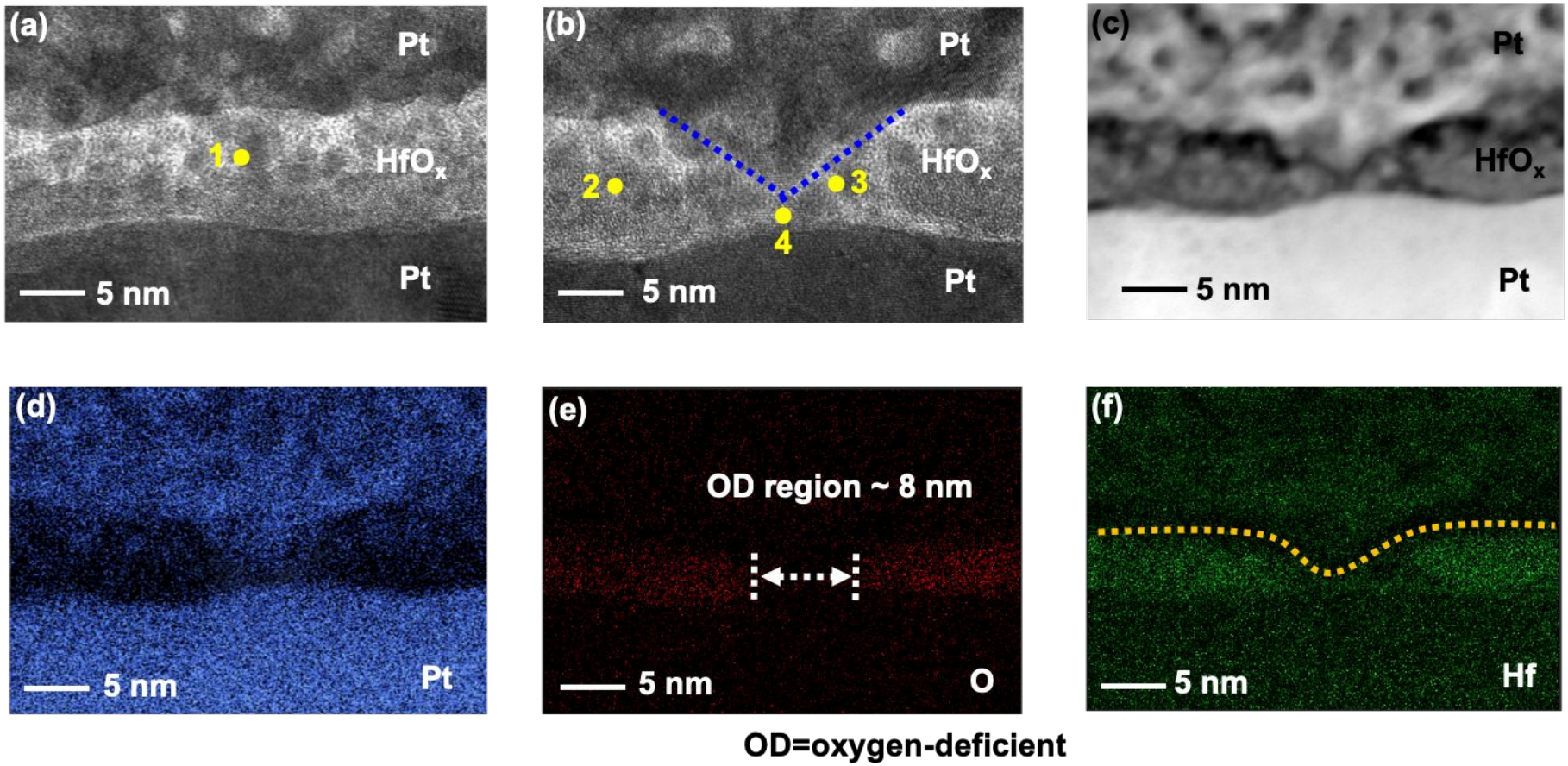

Figure 3. High resolution transmission electron microscope images of the Pt/HfO_x/Pt resistive switching devices with (a) flat HfO_x/Pt interface and (b) inward conical Pt electrode protrusion, respectively. (c) Scanning transmission electron microscope image and (d-f) energy-dispersive spectroscopy mapping of the Pt (L), O (K) and Hf (L) edges of the device with cone-shaped Pt electrode protrusion, respectively.

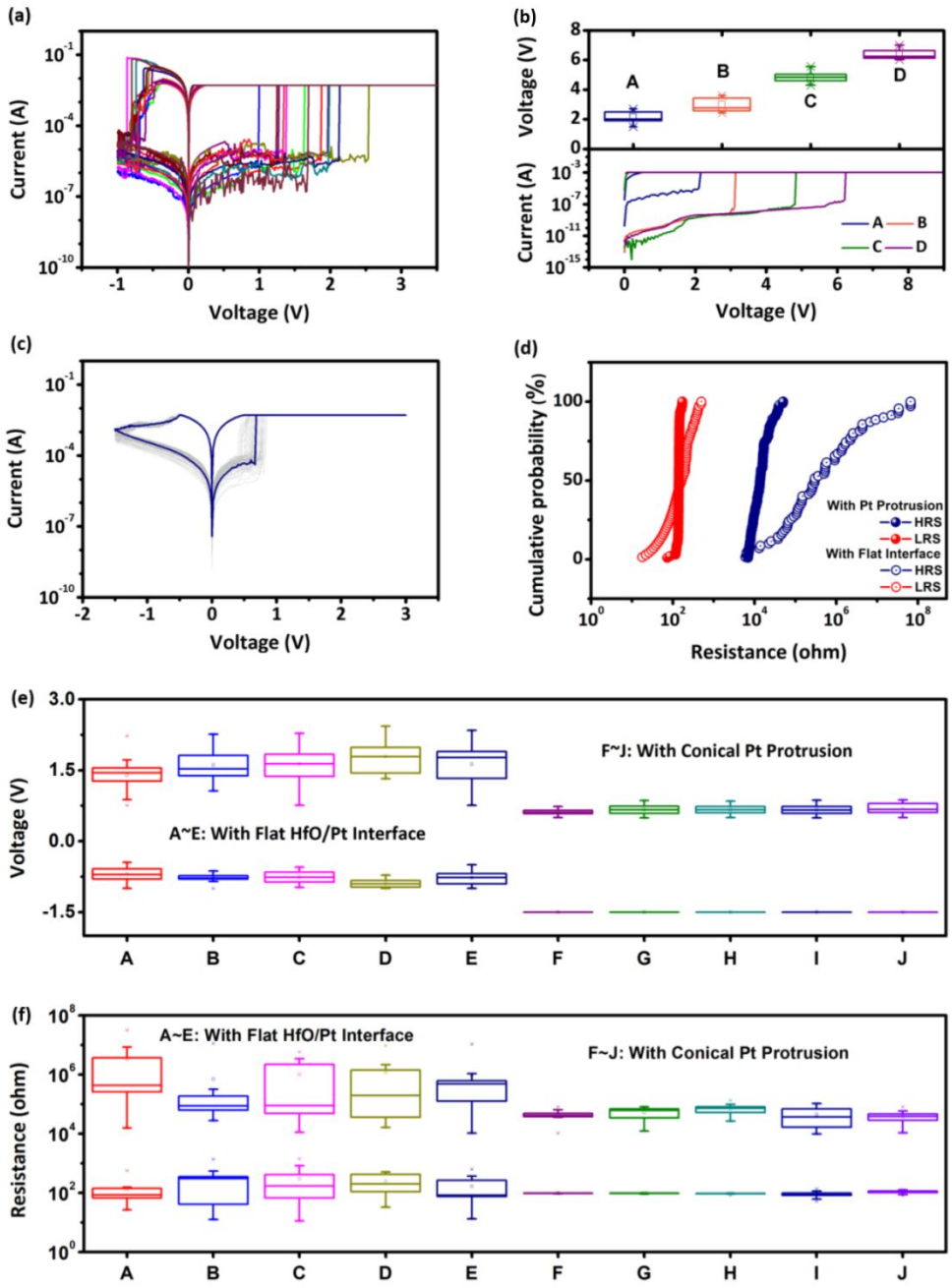

Figure 4. (a) Resistive switching characteristics of the Pt/HfO_x/Pt device with flat HfO_x/Pt interface. (b) Forming characteristics and voltage distribution of Pt/HfO_x/Pt devices with different geometries and hafnium oxide thickness. Sample A is the device with inward conical Pt electrode protrusion and hafnium oxide thicknesses of 10 nm. Samples B to D are devices with flat HfO_x/Pt interface but different hafnium oxide thicknesses of 6 nm, 8 nm and 10 nm, respectively. (c) Resistive switching characteristics of the Pt/HfO_x/Pt device with inward conical Pt electrode protrusion. (d) Cumulative probability of the ON/OFF resistances over 200 cycles, device-to-device variation of the (e) switching voltages and (f) ON/OFF resistances of the

Pt/HfO_x/Pt devicewith flat HfO_x/Pt interface and inward conical Pt electrode protrusion, respectively.

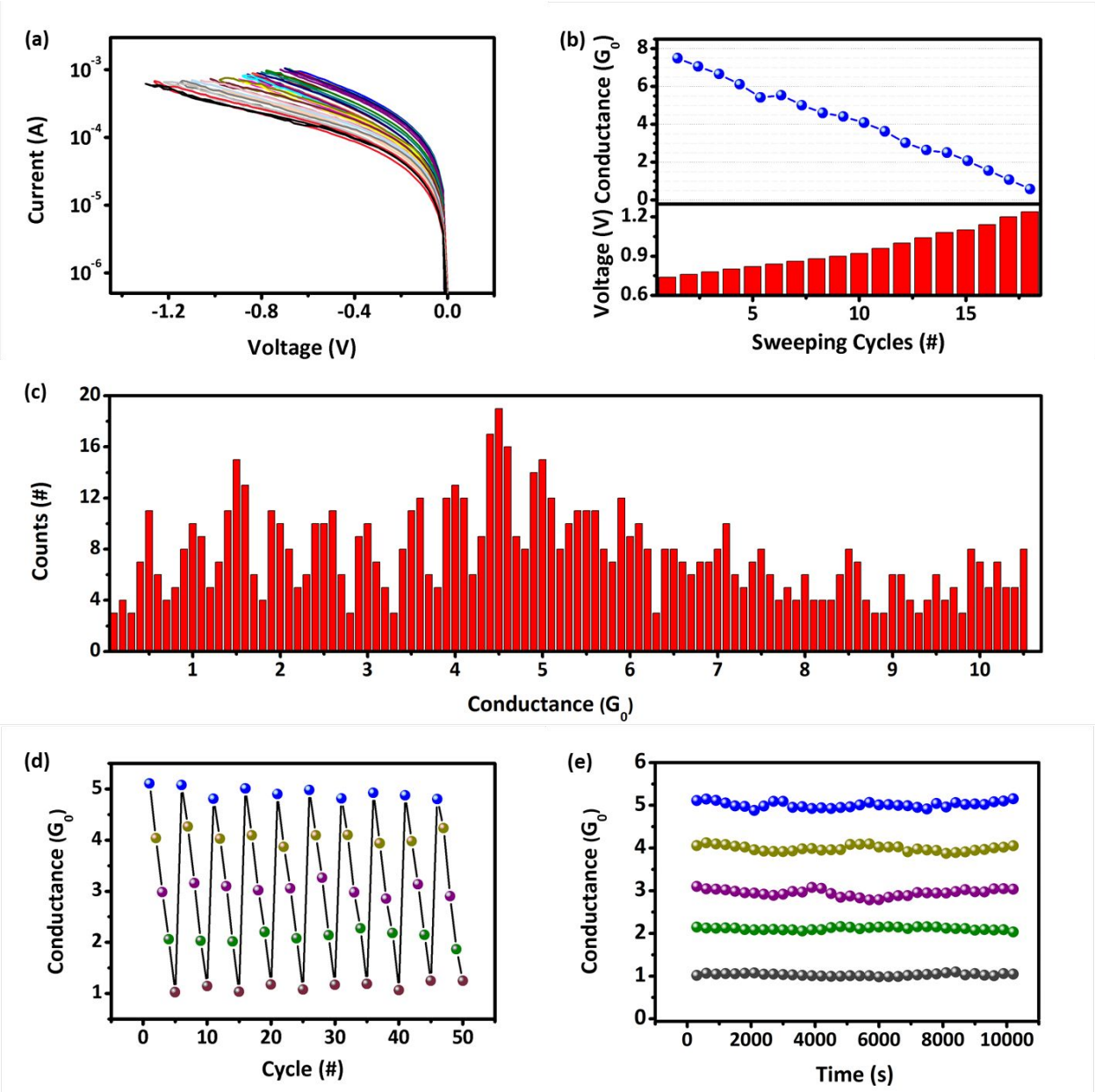

Figure 5. (a) Current-voltage characteristics of the Pt/HfO_x/Pt device with inward cone Pt electrode protrusion showing continuous modulation of device conductance. (b) Evolution of the device quantized conductance and the applied sweeping voltage maximum as a function of the sweeping cycles. (c) Histogram of the device quantized conductance obtained from ~ 800 reset processes. (d) Cyclic tolerance of quantized conductance between $1G_0$ and $5G_0$. (e) Room-temperature retention performance of the quantized conductance states.

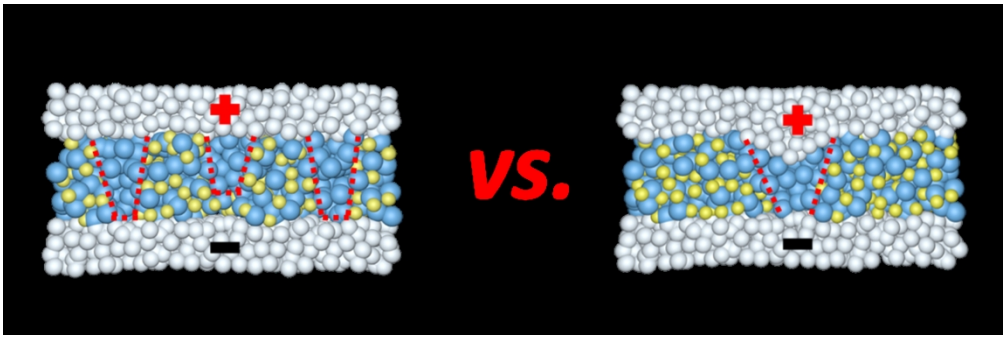

TOC Graphic

192x63mm (300 x 300 DPI)